Dynamics of Gap-Leaping Western Boundary Currents with Throughflow Forcing

CHARLES W. McMahon, a Joseph J. Kuehl, and Vitalii A. Sheremet

^a Department of Mechanical Engineering, University of Delaware, Newark, Delaware ^b Graduate School of Oceanography, University of Rhode Island, Narragansett, Rhode Island

(Manuscript received 1 September 2020, in final form 13 April 2021)

ABSTRACT: The dynamics of gap-leaping western boundary currents (e.g., the Kuroshio intrusion, the Loop Current) are explored through rotating table experiments and a numerical model designed to replicate the experimental apparatus. Simplified experimental and numerical models of gap-leaping systems are known to exhibit two dominant states (leaping or penetrating into the gap) as the inertia of the current competes with vorticity constraints (in this case the β effect). These systems are also known to admit multiple states with hysteresis. To advance toward more realistic oceanographic scenarios, recent studies have explored the effects of islands, mesoscale eddies, and variable baroclinic deformation radii on the dynamical system. Here, the effect of throughflow forcing is considered, with particle tracking velocimetry (PTV) used in the laboratory experiments. Mean transport in or out of the gap is found to significantly shift the hysteresis range as well as change its width. Because of these transformations, changes in throughflow can induce transitions in the gap-leaping system when near a critical state (leaping-to-penetrating/penetrating-to-leaping). Results from the study are interpreted within a nonlinear dynamical framework and various properties of the system are explored.

KEYWORDS: Barotropic flows; Boundary currents; Currents; Mesoscale processes

1. Introduction

a. Motivation

Currents forming along the boundaries of the oceans are strong and ubiquitous. In select locations, such boundary currents encounter a gap in their supporting boundary, resulting in a scenario where the current must traverse the gap, either by leaping across it or by penetrating into it. The nature and variability of these configurations have important influences on the basin that is connected to the larger ocean through the gap. Examples of such situations are the Kuroshio traversing the Luzon Strait of the South China Sea and the Gulf Stream forming the Loop Current in the Gulf of Mexico. These gaptraversing systems are the dominant physical drivers of circulation in the regions they occupy. Catastrophic events (hurricanes, oil spills, etc.) and regional processes caused by their dynamics effect ecosystems, weather, climate, and humanity (National Academies of Sciences, Engineering, and Medicine 2018). The environmental system most relevant to this research is the Kuroshio intrusion.

The Kuroshio is a strong western boundary current (WBC) that forms in the North Pacific Ocean near the Philippines (Nitani 1972). The Kuroshio travels north along the coast of the Philippines with a depth of about 1000 m and an average transport of 21 Sv (1 Sv $\equiv 10^6\, \text{m}^3\, \text{s}^{-1}$) (Centurioni et al. 2004; Yaremchuk and Qu 2004; Nan et al. 2013). It encounters the Luzon Strait, which is a gap in its supporting boundary. The Luzon Strait is the area between the islands of Luzon and Taiwan, and connects the North Pacific Ocean to its east with the South China Sea to its west. The Kuroshio must traverse the gap and takes different paths, as summarized by Caruso et al. (2006). It leaps across the gap the majority of the time, but

Corresponding author: Joseph Kuehl, jkuehl@udel.edu

can also intrude, forming an anticyclonic looping current in the South China Sea (Nitani 1972; Yuan et al. 2006). Eddies are also generated with strong interannual and seasonal variability (Qiu and Lukas 1996). Despite many details of the Kuroshio intrusion being characterized, the intrusion process and its controlling dynamical mechanisms, and interactions between those mechanisms, are not fully understood (Nan et al. 2015). Many of the open problems regarding the Kuroshio intrusion are similar to those of the Loop Current in the Gulf of Mexico.

b. Dynamics of gap-traversing boundary currents

Several theories have been proposed to explain Kuroshio intrusion variability and its dynamical mechanisms. The major theories deal with the effects of wind forcing, mesoscale instabilities, eddy activity, and inertia. Wind forcing has been shown to have an effect on seasonal variation of the Kuroshio intrusion (Qiu and Lukas 1996; Nan et al. 2011) as well as the inertia of the Kuroshio upstream of the Luzon Strait (Centurioni et al. 2004; Wu and Hsin 2012; Hsin et al. 2012). Farris and Wimbush (1996) related transitions from leaping to penetrating states to the accumulation of local wind stress exceeding a critical value. Metzger and Hurlburt (2001) proposed that Kuroshio penetration and eddy development are nondeterministic on longer time scales because of mesoscale instabilities. Further, Yuan et al. (2006) showed that the variability in Kuroshio intrusion is heavily influenced by perturbations due to mesoscale eddies. In an idealized model, Sheremet (2001) showed that if the incoming WBC had enough inertia, it could overcome the vorticity barrier presented by the gap and leap the gap with little to no penetration. Sheremet also showed that the flow exhibits hysteresis. That is, transitions between penetrating and leaping states do not occur at the same flow rate for increasing or decreasing flow rates. This phenomenon of hysteresis in simplified gap-traversing systems has been studied subsequently through laboratory experiments coupled with

numerical models (Sheremet and Kuehl 2007; Kuehl and Sheremet 2009, 2014; McMahon et al. 2020). This hysteresis may be a large factor in the unpredictability of gap-traversing systems in the ocean, if it is indeed present in the environmental systems.

In addition to the historical and experimental investigations mentioned above, significant numerical progress has been made using 1.5-layer reduced-gravity numerical models. Wang et al. (2010) studied the effect of meridional wind stress. As meridional wind stress decreases from a positive value, the hysteresis range widens and shifts to higher WBC transport. The authors noted that the trends are similar for the Kuroshio intrusion, where in the winter northerly winds persist and penetrating states are more common. In the summer, southerly winds are more common, and penetrating states rarely occur. Yuan and Wang (2011) and Lien et al. (2014) studied the effect of mesoscale eddies impinging from the east. In the former, eddies were found to induce transitions of the WBC path when the system is near a critical state, as the eddies act to reduce or enhance inertial advection of vorticity. Song et al. (2019) primarily studied the effect of periodic variation in WBC transport. For the increased period, the hysteresis range increased. In addition, Song et al. briefly studied the mean leakage of the WBC through the gap. It was found that this mean throughflow must be greater than one-third of the transport of the WBC in order to have an effect on the hysteresis range. For increasing throughflow, the hysteresis span is shown to move left (to lower transport), so that leaping states are more common. Mei et al. (2019) studied the influence of an island in the gap. Overall, the presence of an island facilitates penetration of the WBC into the gap. A vorticity balance analysis confirms that transitions occur as a result of increased/decreased meridional advection. Additionally, the influence of an eastward-shifted island is gradually reduced when the island is east of the Munk layer. Last, Yuan et al. (2019) studied how mesoscale eddies from the east propagate through the gap. A leaping WBC pattern blocks almost all eddies from propagating through the gap. In contrast, eddies easily travel through the gap when the WBC is in a penetrating state. The eddies can influence the WBC flow in the gap when near transition points, consistent with Yuan and Wang (2011).

The literature reviewed shows the discovery of hysteresis in simplified gap-traversing systems, the development of the cusp catastrophe dynamical framework, the inclusion of characteristics that are exhibited in oceanographic scenarios, and the persistence of hysteresis under these added complexities. In addition to those listed above, there is the opportunity to include more relevant oceanographic effects to these models. For the Kuroshio intrusion, there is often a significant net transport directed westward or eastward through the Luzon Strait.

c. Throughflow problem

Wyrtki (1961) provided some of the first evidence of the Kuroshio east of Taiwan and documented its seasonality (peaking near May and minimum near November). Wyrtki also provided/summarized some of the first evidence of Luzon Strait transport (LST). Qiu and Lukas (1996) considered Kuroshio transport variations due to seasonal wind patterns

and variation in the North Equatorial Current bifurcation location and found similar results to Wyrtki. Centurioni et al. (2004) reached similar conclusions using 15-m drogued drifters, and found a lack of Kuroshio intrusion during high Kuroshio transport month and the presence of Kuroshio intrusion during low transport months. More recently, Nan et al. (2015) provided a summary of LST estimates from numerous studies over differing time spans and using varying methods. Most recently, Wei et al. (2019) provided a summary of Pacific to Indian Ocean throughflow (including the South China Sea branch) from observations. LST varies between about 12 Sv westward into the South China Sea and 5 Sy eastward into the Pacific Ocean. The average LST is between 3 and 6.5 Sv westward. For comparison, the inflow Kuroshio averages a transport of 21 Sv, ranging between about 15 and 25 Sv (Nan et al. 2013). One of the paths of the Kuroshio intrusion identified in Caruso et al. (2006) is the South China Sea branch of the Kuroshio (SCSBK), which flows into the South China Sea and southwestward along the shelf break of China, while the majority of the Kuroshio leaps directly across the Luzon Strait. Even when the Kuroshio leaps across the gap, there still may be LST into the South China Sea due to the SCSBK. When the Kuroshio intrusion is at a penetrating state, there is also a potential for westward LST. The theorized drivers of LST vary by study, with some examples being wind stress (Liu et al. 2010), interbasin pressure gradient (Nan et al. 2013), and coupling with the Indonesian throughflow (Liu et al. 2006). The LST has been weakening over the past two decades (Nan et al. 2013). If the LST has an effect on the dynamics of the Kuroshio intrusion, this weakening may affect trends of the system. Given the possibility for a significant amount of Luzon Strait transport, it should be considered how throughflow forcing may affect the dynamics and hysteresis of gap-traversing systems. The effect of a positive or negative mean throughflow through the gap will be studied in single-layer laboratory experiments, and a numerical model designed to replicate the experimental apparatus.

This manuscript is organized as follows. Section 2 describes the models and methods used to study gap-traversing western boundary currents. Section 3 presents general results from the experiments on the presence of throughflow. Section 4 analyzes and discusses these results. Section 5 provides a summary and conclusions in the context of historical work and the Kuroshio intrusion. An appendix contains the more traditional formulation of the problem.

2. Methods

To study the dynamics of gap-leaping western boundary currents with the effect of throughflow, a simplified rotating table laboratory experiment and equivalent numerical model are devised. As mentioned before, previous studies have used rotating table experiments to study gap-leaping boundary currents, both in the single-layer and two-layer cases (Sheremet and Kuehl 2007; Kuehl and Sheremet 2009, 2014). Here only a single layer setup will be considered. The model will be a primarily inertial boundary current, which mimics the Kuroshio (Stommel and Yoshida 1972). Particle tracking velocimetry (PTV) will be

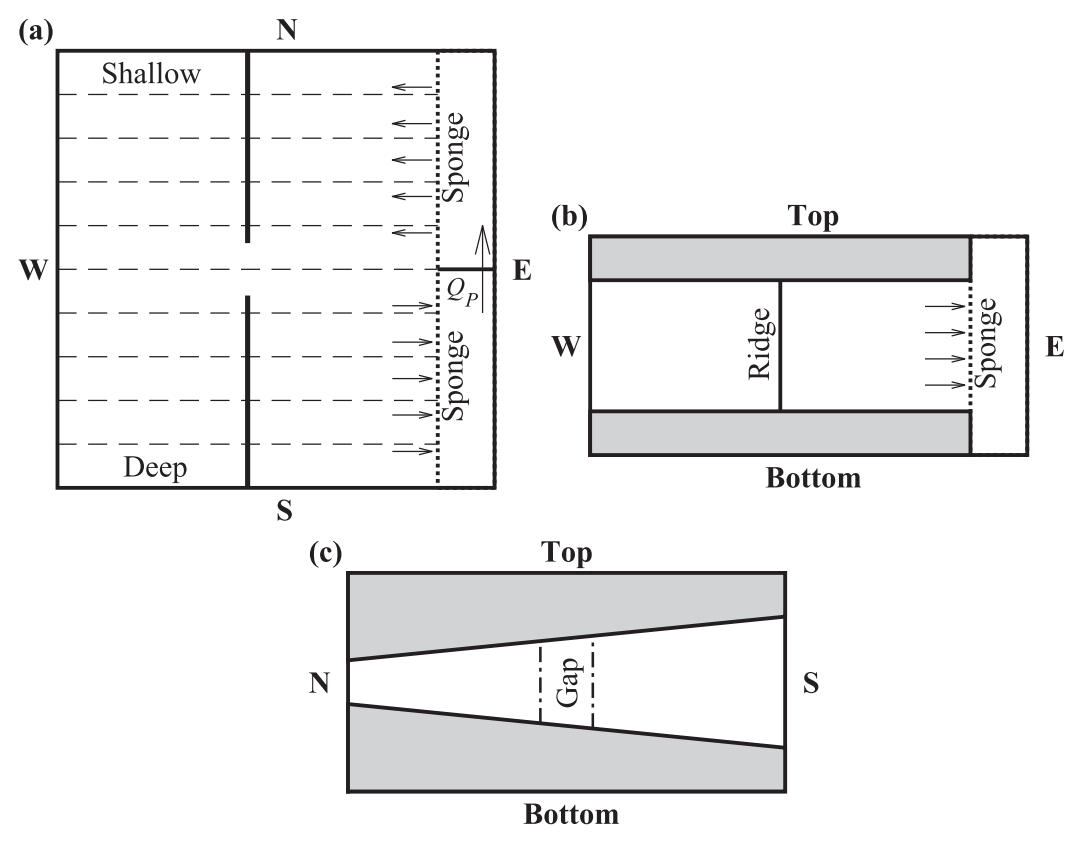


FIG. 1. Top and side views of the rotating table tank. (a) Top view; dashed lines are constant fluid layer thickness contours; Q_P is the flow rate of the primary pump that induces the tank circulation. (b) South view. (c) West view.

used to obtain time-resolved volumetric velocity fields and subsequent data from the laboratory experiments.

a. Laboratory model

The laboratory model is created with features that mimic the general oceanographic scenario of a gap-leaping WBC (e.g., β effect). The laboratory setup used is like that of Kuehl and Sheremet (2014), but exclusively the barotropic case. A square tank of sides 1 m and height 0.5 m is placed on a rotating table that is set to rotate at a constant rate $\Omega = 0.65 \,\mathrm{rad\,s^{-1}}$. The tank is divided into different compartments containing appropriate geometries (Fig. 1) and pump forcing configurations (Fig. 2). North and south (y axis), and east and west (x axis) directions are introduced in analogy to the oceanographic scenario, and the origin is placed in the middle of the gap in the ridge. Figure 1 shows most of the tank consisting of an active fluid layer bounded by a sloping rigid lid and a sloping bottom. These sloping boundaries, each with slope S = 0.1, act opposite to each other to create a linear variation of the fluid layer depth in the y direction, which imparts a topographic β effect on the rotating fluid layer. The shallowest part is in the north and the deepest is in the south. With a layer thickness of $H_0 = 20$ cm at the center depth contour, the fluid depth is $H(y) = H_0 - 2Sy$.

A 6-mm-thick vertical ridge (reaching from the bottom to the lid) is situated in the north-south direction to divide the active fluid region in half, shown in Fig. 1. The two basins are $L_b = 43.5$ cm wide in the x direction. The basins are the full $L_t = 100$ cm wide in the y direction. A gap is in the center of the ridge with a total width $L_g = 12$ cm and a half-width a = 6 cm, and the edges of the ridge are rounded. A forcing region of width 13 cm occupies the eastern part of the tank and consists of two sponges separated by a divider. Pumping through these sponges creates the circulation that results in a western boundary current forming along the vertical ridge. Flow is driven by the primary pump at volumetric flow rate Q_P from behind the southern sponge to behind the northern sponge. The pressure difference across the inflow sponge induces fluid to percolate out of the sponge forming a broad Sverdrup interior flow as it follows depth contours toward the west. As this interior flow encounters the ridge to its west, it forms a southward flowing boundary current. This occurs under the influence of the topographic β effect of the tank which is analogous to the planetary β effect of ocean currents. The WBC must then negotiate the gap in the ridge before reaching the southern part of the basin where it is recirculated through the outflow sponge. Flow inertia of the WBC will induce the current to leap across the gap while the β effect will induce the current to penetrate into the gap (sketched in Fig. 2). A "southward" flowing boundary current is created here. This is permitted because in the barotropic case there is a north-south invariance of the quasi-geostrophic dynamics, which was

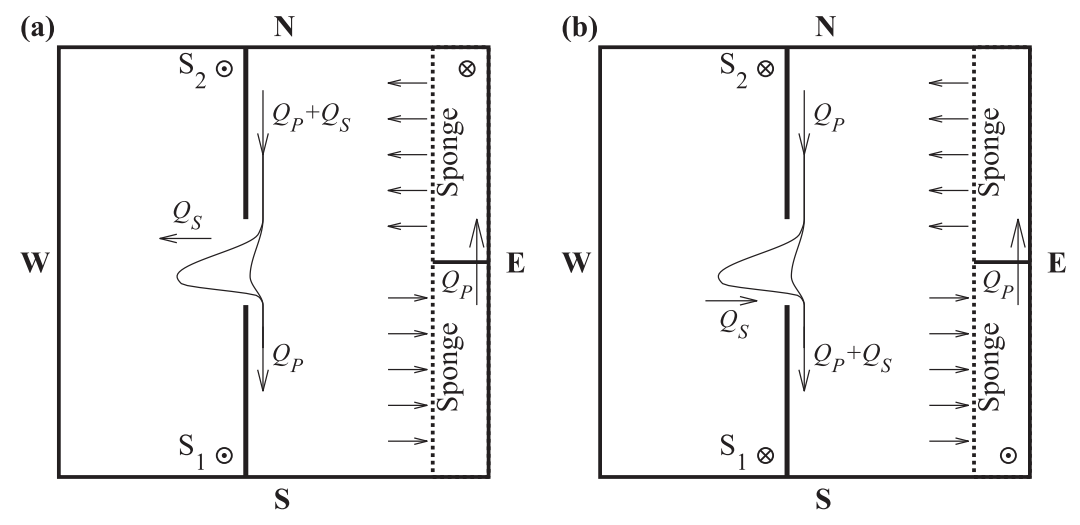


FIG. 2. Pumping configurations of the laboratory model that induce positive or negative throughflow. S_1 and S_2 mark the two possible sink–source locations. A schematic of penetrating/leaping states is included. (a) Positive throughflow; here Q_S is the flow rate of the secondary pump which pumps from either S_1 or S_2 to behind the northern sponge; so the inflow WBC transport is $Q_P + Q_S$ and the throughflow is Q_S into the western basin. (b) Negative throughflow; here Q_S is the flow rate of the secondary pump which pumps from behind the southern sponge to either S_1 or S_2 ; so the inflow WBC transport is Q_P and the throughflow is Q_S out of the western basin.

confirmed by Kuehl and Sheremet (2014) for a similar tank geometry. This also results in an increasing layer thickness in the downstream direction as in the oceanic boundary current case.

THROUGHFLOW MODEL

Throughflow forcing is included in this laboratory model of a gap-leaping WBC by introducing a secondary pump that moves fluid between the western basin and the forcing region in the east (Fig. 2). Experiments were run for both positive throughflow out of the gap westward (Fig. 2a) and negative throughflow eastward into the WBC basin (Fig. 2b). In both cases, there are two options for sink-source locations in the western basin: one in the southeastern corner (S_1) and the other in the northeastern corner (S_2) . One end of the tubing connected to the secondary pump is inserted through a hole in the rigid lid at either S_1 or S_2 , and the other hole not in use is plugged. The tube is inserted into most of the thickness of the layer at the sink-source location and the end of the tube has holes cut in it to dilute the flow. The other end of the tubing is placed behind the northern forcing sponge for positive throughflow and is placed behind the southern sponge for negative throughflow. With the secondary pump (throughflow) rate being Q_S , these four possible flow configurations are shown in Fig. 2. The weak circulations resulting from the forcing are plume flows diverging off the northern ridge edge for positive throughflow, or converging toward the southern ridge edge for negative throughflow (shown by arrows for Q_S in Fig. 2). Due to the configurations, the incoming WBC transport is $Q = Q_P + Q_S$ for the positive throughflow case and $Q = Q_P$ for the negative throughflow case. The throughflow forcing $Q_{\rm TF} = Q_S$ (positive westward) will be the main independent variable in the study. When plotting and analyzing results, we will always consider the WBC transport unless specifically stated, as this is most relevant to the oceanographic problem.

b. Numerical model

The numerical model utilized in this study is a barotropic version of the baroclinic model developed to support a series of rotating table laboratory experiments (Sheremet 2001; Sheremet and Kuehl 2007; McMahon et al. 2020) Both the experimental setup and validation of the numerical model have been well established in the literature (McMahon et al. 2020; McMahon et al. 2020, manuscript submitted to *Ocean Modell.*), so only a brief summary is provided here.

In nondimensional form, the problem is formulated as the steady potential vorticity advection–diffusion equations

$$J(\psi, q) + \lambda_S \frac{1}{h} \omega - \lambda_M^3 \nabla^2 \omega = 0,$$

$$-\nabla \left(\frac{1}{h} \nabla \psi\right) - \omega = 0,$$
 (1)

where ψ is the transport function, $\omega = \nabla \times \mathbf{u}$ is the relative vorticity, $q = (1/\hat{\beta} + \lambda_I^2 \omega)/h$ is the potential vorticity with $h = 1 - \hat{\beta}y$ (see appendix for further details). The nondimensional parameter $\hat{\beta} = \beta L/f = SL/H_0$ is the relative meridional variation of depth over the basin due to the sloping bottom, h is the fluid depth, and g is gravity. The domain is $-L_b/(0.5L_t) < x < L_b/(0.5L_t)$, -1 < y < 1. The kinematic conditions for solving the elliptic equation are $\psi = 0$ along all boundaries, except at the eastern boundary $x = L_b/(0.5L_t)$ where inflow/outflow is prescribed $\psi = \Psi_B(y)$, with Ψ_B varying between 0 and 1. The dynamical conditions are noslip: v = 0 at the western $x = -L_b/(0.5L_t)$, eastern $x = L_b/(0.5L_t)$ boundaries and along the ridge; and no-stress $\omega = 0$

at the southern y=-1 and northern y=1 boundaries. The resulting parameters $\lambda_I=\sqrt{U_0/\beta L}, \lambda_S=k_0/\beta L$ with $k_0=f(h_E/H_0)$, and $\lambda_M=(\nu/\beta L)^{1/3}$ are the nondimensional inertial, Stommel, and Munk boundary layer thicknesses as in standard quasigeostrophic theory; U_0 is the Sverdrup interior velocity scale, L is the basin length scale, h_E is the Ekman depth (defined in the appendix), and ν is the kinematic viscosity.

The numerical problem is solved using standard finite differences on a rectangular grid dividing the domain into $N_r \times$ N_v cells. The parameters λ_s and λ_M represent dissipative effects, while λ_I characterizes the nonlinearity, i.e., the strength of the flow. For small boundary layer Reynolds numbers R = $(\lambda_I/\lambda_M)^3$, simple explicit iterations, treating the nonlinear terms as perturbations, work well, but for the moderate R the iterations fail to converge. In this case Newton's method has be to employed to find steady solutions. We consider a state vector $\mathbf{X} = (\omega, \psi)$ consisting of values at all grid nodes including the boundaries; the size of this vector is $M = (N_x + 1) \times (N_y + 1) \times$ 2. Substituting an initial guess X_0 into 1 results in the vector of residuals $F(\mathbf{X}_0)$ at each grid node of the same size M. To find \mathbf{X}_1 that brings residual closer to vanishing $F(\mathbf{X}) = 0$, we need to calculate the Jacobian matrix $\mathbf{J}_F[\mathbf{X}_0]$ (of size $M \times M$, which depends on X_0) of all first-order partial derivatives of F with respect to X and then solve the linear system

$$\mathbf{J}_{F}[\mathbf{X}_{0}](\mathbf{X}_{1} - \mathbf{X}_{0}) = -F(\mathbf{X}_{0}). \tag{2}$$

The iterations then continue until the residual completely vanishes. The elements of the Jacobian matrix can be calculated analytically by considering the variational problem corresponding to (1):

$$\begin{split} \mathbf{J}(\delta\psi,q) + \mathbf{J}(\psi,\delta q) + \lambda_S \frac{1}{h} \delta\omega - \lambda_M^3 \nabla^2 \delta\omega &= 0 \,, \\ - \nabla \bigg(\frac{1}{h} \nabla \delta\psi \bigg) - \delta\omega &= 0 \,, \end{split}$$

where $\delta q = \lambda_I^2 \delta \omega / h$. The variations of the boundary conditions are trivial. It should be noted that the elements of the Jacobian matrix do not have to be calculated exactly. As long as the iterations converge and the residual $F(\mathbf{X})$ vanishes, we get an exact solution to the original problem 1. Finite difference approximations result in a sparse banded type of \mathbf{J}_F , and the grids of size up to 1000×1000 can be solved on a computer with 24 GB of operational memory.

c. Procedure

The goal of one experimental run is, for a single (positive or negative) throughflow rate Q_{TF} , to cycle through a hysteresis trace of the system, imaging velocity fields or exporting numerical output throughout the process. WBC transport is first set to a low flow rate, so that the current penetrates into the gap. Then the transport is gradually increased until the state changes to leaping. The process is then reversed until the system transitions to penetrating again. In the laboratory model, care must be given to let the system equilibrate to a steady or quasi-steady (eddy shedding) state after changing the flow rate before imaging the current. The record length of imaging must

also be long enough to capture any variability of the system (i.e., longer than the eddy shedding period, if it exists). In the laboratory, flow is measured using particle tracking velocimetry (PTV) with four cameras mounted above the tank and with particles seeding the flow. An established procedure is used to ensure the accuracy of the resulting time-resolved volumetric velocity fields. Dye visualization was used for scoping runs to determine best experimental parameters, to verify that the Sverdrup inflow from the inflow sponge is uniform, and to verify that the rotation of the table was constant with no disturbances.

1) LABORATORY PROCEDURE

The laboratory procedure begins with filling an open storage tank with warm water and letting it cool to room temperature (≈20°C). Warm water contains less dissolved gases that would otherwise increase the formation of bubbles on the rigid lid, which negatively affects the accuracy PTV visualization. The experimental tank is then filled and seeding particles are introduced. The forcing sponges are inserted and saturated, and the pumps are arranged into the correct configuration. The table and tank are then rotated at rate Ω , and the fluid is allowed enough time to reach solid-body rotation with no flow (about 20 min). Forcing is then initiated with the primary pump at a low flow rate and with the secondary pump at the prescribed flow rate. The system is allowed to reach a steady or quasi-steady (eddy shedding) penetrating state. The flow is then imaged. The primary pump flow rate Q_P is increased by $1.67 \,\mathrm{cm}^3 \,\mathrm{s}^{-1}$, and the current is allowed to equilibrate for about 5-10 min. This is repeated until the flow nears the critical transition state. Then a flow step size of 0.83 cm³ s⁻¹ is repeated until the system transitions to a leaping state. This process is then repeated for decreasing flow rates until the system transitions back to a penetrating state. For the given pump configuration, varying throughflow rates $Q_{TF} = Q_S$ are prescribed to achieve a set of hysteresis traces. This is done for all four combinations of sink-source location and positive or negative throughflow.

2) PARTICLE TRACKING VELOCIMETRY

Images of the evolution of the seed particles were recorded using four CCD cameras (MiniShaker L, LaVision, Germany) of 1984×1264 resolution each. The lenses of the cameras were 1:1.6/8 mm (HF8XA-5M, Fujinon). Prior to experiments, the cameras were calibrated by inserting a calibration plate into the center of the flow domain and area of interest. This orients the cameras relative to each other while viewing through the tank media. Additionally, the experimental setup has fluid on top of the rigid lid (not impacting the flow domain). Therefore a window was created to eliminate the parabolic free surface, which would otherwise cause problems in calibration. For the experiments, the fluid was seeded with about 4 mL of 60-µm spherical polyamide particles. A timing unit was used to control the pulses of an LED array (LED-Flashlight 300, LaVision, Germany) to illuminate the particles. The light array was directed horizontally from the west side of the tank and was restricted using black paper to illuminate the volume of interest. The cameras and light source were triggered to

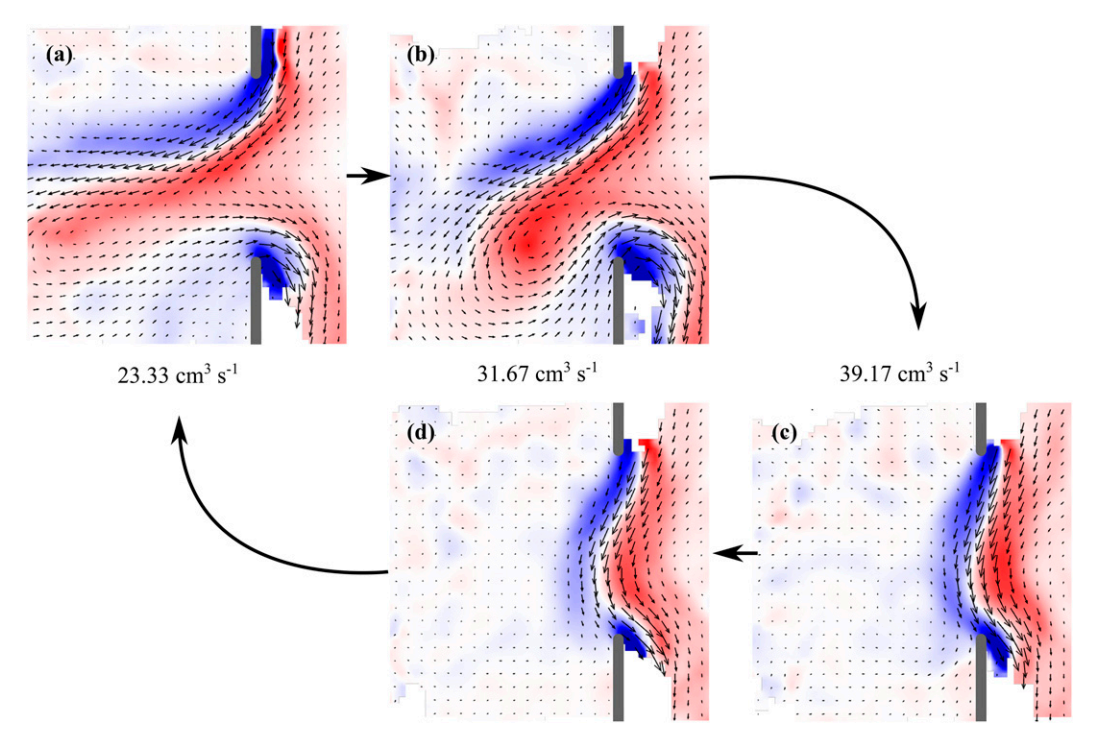


FIG. 3. Laboratory mean velocity fields for the zero throughflow case, illustrating hysteresis in the system as WBC transport is varied. The red/blue color map is relative vorticity strength. (a) Starting with a low flow rate, the system admits a deep penetrating state. (b) As the flow rate is increased, the looping current shrinks and becomes more defined. (c) As the flow rate is increased more, the current abruptly transitions to a leaping state. (d) The flow rate is then decreased, yet a leaping state persists, even for the flow rate of (b), showing the existence of multiple states. As the flow rate is decreased further, the current eventually transitions abruptly from a leaping state to the penetrating state in (a).

image the flow at a rate of about 4 Hz. This imaging frequency was determined from the PTV algorithm guide that particles should move a maximum of about 10 pixels per frame in the resulting image sequence for the slow flow under study. After preprocessing steps such as masking and filtering of the raw particle images, and after further refining the calibration using volume self-calibration, particle tracks were calculated using a PTV algorithm (Shake-the-Box, LaVision, Germany). The particle tracking result is then converted to a grid for time-dependent volumetric velocity fields of the gap-leaping WBC. Postprocessing is applied to these vector fields to obtain measurements such as vorticity fields and average velocity fields.

3) Numerical procedure

In the numerical model, flow rates are varied to achieve a hysteresis trace similar to the laboratory procedure. The rough flow rate step size was 1.67 or 3.33 cm³ s⁻¹, while the step size used when nearing a state transition was reduced. Due to the use of Newton's method, once the gap-traversing WBC reaches a transition point the model will fail to converge because the current solution branch turns/disappears. Additionally, eddy shedding states will not occur because a steady-state model is used. For increasing flow rates, the series of flow rates begins with solid-body rotation and continues until the critical penetrating state is reached. For

decreasing flow rates, a leaping state initial condition must be constructed. A flow solution is determined for a small 2-cm gap width for a high flow rate (greater than the determined critical penetrating state flow rate). This forces the state of the system to be leaping. The gap width is then stepped up gradually over successive model runs until it reaches the full 12-cm gap width, thus creating the starting leaping state. The flow rate is then decreased gradually until the critical leaping state is achieved, signified by no convergence.

3. Results

a. Hysteresis

Both the laboratory and numerical models exhibited hysteresis as expected. Figure 3 shows laboratory mean velocity fields as the strength of the boundary current (Q) is varied for zero throughflow $(Q_{\rm TF}=0)$. Starting at $23.33\,{\rm cm}^3\,{\rm s}^{-1}$, the current is in a penetrating state. This is because the WBC does not have enough inertia to overcome the vorticity barrier to leap across the gap. As the flow is steadily increased to $31.67\,{\rm cm}^3\,{\rm s}^{-1}$, the extent of the penetration decreases and the looping current becomes more resolved. The loop current also tilts southward because the increased inertia allows it to cross topographic contours. As the flow is increased further, the

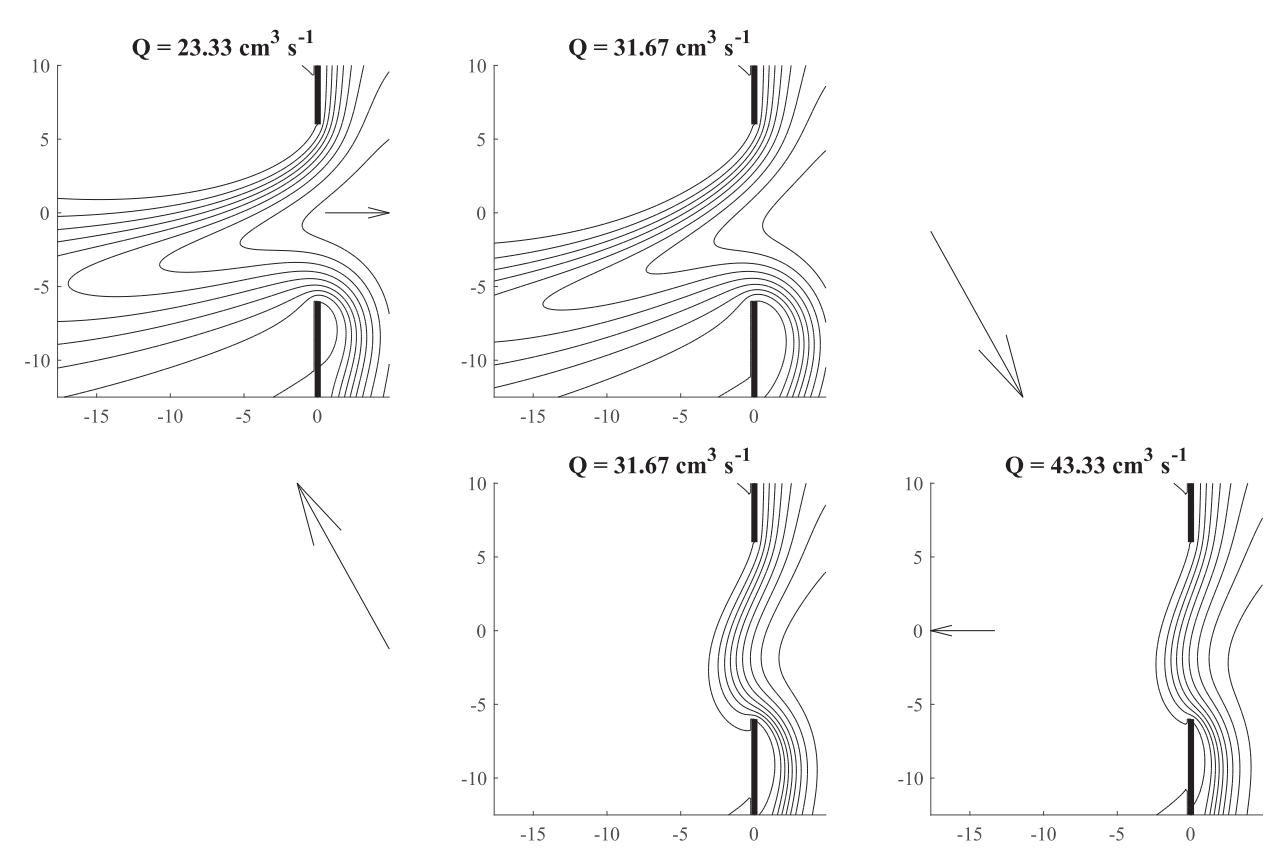


FIG. 4. Numerical model results for the zero throughflow case, illustrating hysteresis in the system as WBC transport is varied. The solid lines are contours of the transport function solution. Arrows indicate how the states are achieved by increasing or decreasing WBC transport. The axes' dimensions are cm, and the flowfield domain window is the same as in Fig. 3.

system reaches a critical penetrating state and then abruptly transitions to a leaping state. The inertia has overcome the vorticity barrier. A leaping state is shown for $39.17\,\mathrm{cm^3\,s^{-1}}$. Then, as the flow is steadily decreased back to $31.67\,\mathrm{cm^3\,s^{-1}}$, the leaping state persists. This occurs for flow rates that previously resulted in penetrating states, therefore multiple states occur depending on whether the flow is increasing or decreasing (hysteresis). As the flow is decreased further, the system reaches a critical leaping state and then abruptly transitions back to a penetrating state for sufficiently low flow.

Similarly, Fig. 4 shows the results of the numerical model for zero throughflow. Contours of the numerical transport function solution are plotted, and arrows show how the systems evolve for varying WBC transport. A state variable measuring the size of the loop current can easily be calculated from the numerical results. The transport line $\psi = (2/5)Q$ is used for calculation because it lies in the core the incoming WBC. Parameter \mathbf{X}_p is the location of the maximum curvature of this transport line, which is calculated relative to the origin at the center of the gap. Thus, the distance of the maximum curvature of this transport line from the origin $(|\mathbf{X}_p|)$ sufficiently measures the size of the loop current. Parameter $|\mathbf{X}_p|$ is plotted versus WBC transport in Fig. 5 for the zero throughflow case to show hysteresis. The penetrating and leaping solution branches are shown to overlap, indicating hysteresis. The decrease in

loop current size is characteristic of the system approaching the critical penetrating state (solid upward triangles in Fig. 5), which terminates the penetrating branch. The increased bending of the leaping WBC is characteristic of the system approaching the critical leaping state (solid downward triangles in Fig. 5), which terminates the leaping branch. The penetrating and leaping solution curves in the hysteresis region resemble the stable solutions of the two folds in a cusp catastrophe surface. Between the two folds (within the hysteresis regime) there exists a third unstable flow state which has been recently calculated by McMahon et al. (2020, manuscript submitted to Ocean Modell.) and provides insight into the fundamental dynamics of gap-leaping systems. Kuehl and Sheremet (2009) identified a cusp catastrophe surface of type A_3 as a suitable framework for a gap-traversing system because the two folds merge as the table rotation rate (controlling the vorticity barrier) is decreased (Gilmore 1981). That is, hysteresis is eliminated for sufficiently small rotation rates and the hysteresis range increases with increasing rotation rates.

b. Dependence on throughflow

For a given hysteresis trace, its range limits are the leaping-topenetrating and penetrating-to-leaping transition WBC transport values. As shown below, a convenient scaling for the strength of

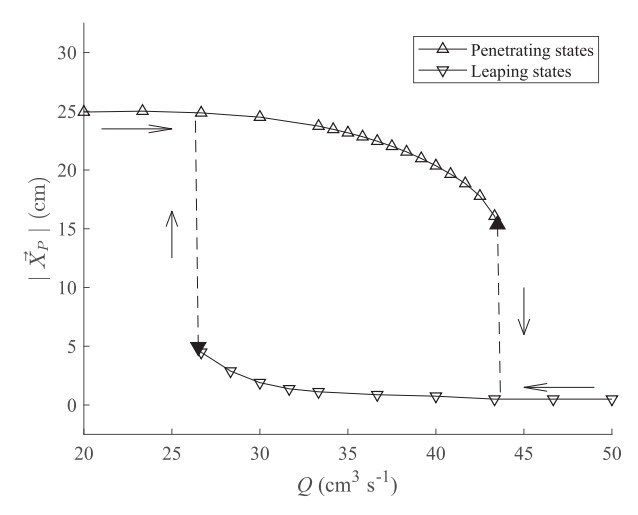


FIG. 5. Numerical model hysteresis trace for zero throughflow. The state variable is chosen as $|\mathbf{X}_p|$, the distance from the origin of the location of the maximum curvature of the $\psi = (2/5)Q$ transport line. Solid triangles represent the critical states just before transition (at Q = 26 and $43 \, \mathrm{cm}^3 \, \mathrm{s}^{-1}$.).

the WBC transport is given by a balance between nonlinear advection and the β effect, and results in a nondimensional coefficient $K = \hat{Q} = Q/(\beta a^3 H_0)$ that quantifies the strength of the WBC. The penetrating-to-leaping transition point K_P is determined from the flow rate of the measured critical penetrating state plus half of the next flow rate step (i.e., halfway between the successive penetrating then leaping state). The K_P may also be framed as the parameter at which the penetrating solution branch terminates as K is increased. The leaping-to-penetrating transition point $K_{,L}$ is determined from the flow rate of the measured critical leaping state minus half of the next flow rate step (i.e., halfway between the successive leaping then penetrating state). The $K_{,L}$ may also be framed as the parameter at which the leaping solution branch terminates as K is decreased. We are interested in how K_{P} and K_{L} change with positive and negative throughflow forcing. The throughflow forcing will be represented by the same coefficient as K'for convenience, with Q being replaced by Q_{TF} .

It is found that positive and negative throughflow significantly affect the hysteresis range of the gap-traversing system. Overall, positive throughflow shifts the hysteresis range to higher WBC values and widens the hysteresis width. Negative throughflow shifts the hysteresis range to lower WBC values and narrows the hysteresis width. Figure 6 shows this throughflow effect for the laboratory model for both sourcesink locations S_1 and S_2 . For a given throughflow value on the x axis, the hysteresis range is shown on the y axis. The K_P values are marked with upward triangle markers and are fit with a linear trend (solid line). The $K_{,L}$ values are marked with downward triangle markers and are fit with a linear trend (dashed line). The trends in both K_P and K_L are positive for increasing throughflow. The x axes show the throughflow K'on a continuum for negative and positive throughflow values. The linear fits of the data are good approximations over the full range of K' observed. For anywhere in the observed K and K'

space, the state of the system can be determined given the found trends in critical parameters. The system is leaping for K above the solid line approximating $K_{,P}$. The system is penetrating for K below the dashed line approximating $K_{,L}$. The region of hysteresis in the system is between the solid and dashed lines, and the state depends on prior evolution of the system.

The slopes of the linear trends for $K_{,P}$ and $K_{,L}$ are significant with values between 0.9 and 1.78. The $K_{,P}$ slopes are greater than the $K_{,L}$ slopes. Additionally the slope trends in the data are enhanced for source–sink location S_2 compared to S_1 .

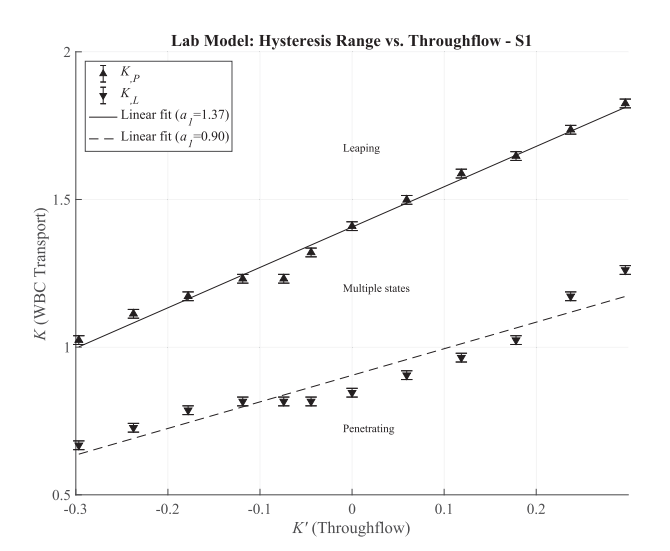
Figure 7 shows the throughflow effect for the numerical model. The results for source–sink S_1 and S_2 were identical for the numerical model, so only one figure is shown. The trends in the data are similar to the laboratory experiments. Linear fits approximate the data very well with slopes of 1.59 and 1.07 for $K_{,P}$ and $K_{,L}$, respectively. The $K_{,L}$ data are consistent with the laboratory results. The $K_{,P}$ data are shifted slightly upward to higher K values compared to the laboratory results. For all model cases, positive throughflow facilitates WBC penetration by shifting the hysteresis range to higher WBC flow rates. Negative throughflow facilitates WBC leaping by shifting the hysteresis range to lower WBC flow rates. The linear trends in these results were significant with slopes of about one or greater.

4. Discussion

a. Effect of throughflow

The trends in $K_{,P}$ and $K_{,L}$ were notably linear for the range of K' examined for all models. The leaping-to-penetrating transition points had a slope of about 1. The penetrating-toleaping transition points had an even greater slope of about 1.5. The linear trends in the data are valid even for small throughflow deviations from the base zero-throughflow case. That is, to the resolution studied here, there appears to be no minimum throughflow magnitude required to have an effect on hysteresis. This sensitivity to throughflow for the barotropic case is contrary to the baroclinic results of Song et al. (2019), which found that the mean throughflow must be greater than one-third of the transport of the WBC in order to have an effect. A possible reasoning for this difference is provided below. The throughflow effects for the laboratory and numerical models of this study were directly proportional and significant. Based on these trends, when the system is near a critical penetrating state, a decrease in throughflow may induce a transition to a leaping state. Similarly, when the system is near a critical leaping state, an increase in throughflow may induce a transition to a penetrating state.

In general, multiple steady states and hysteresis arise in the systems due to the nonlinear effects. In the problem without throughflow, it was shown by Sheremet (2001) that the criteria for the breakdown of the steady solution branch can be derived from scaling arguments. For the β -plume solution flowing out of the gap, the breakdown occurs when the nonlinear advection (directed eastward) becomes comparable to the β effect (carrying flow characteristics westward). This is a hydraulic control on the β plane: the Rossby waves with the meridional scale of



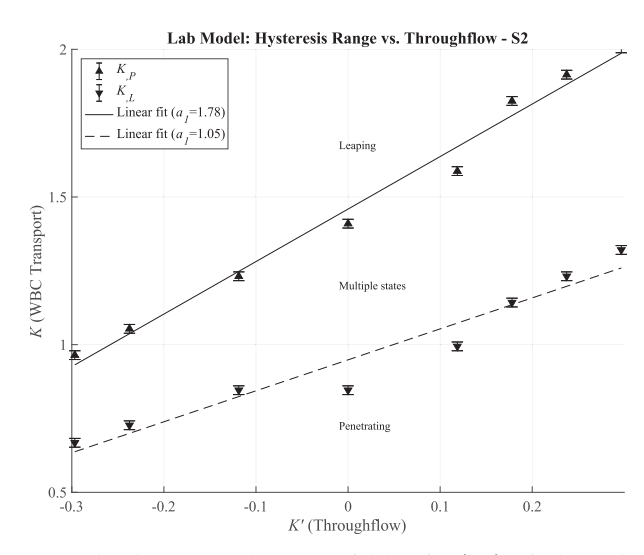


FIG. 6. Laboratory model, source–sink location (top) S_1 in the south and (bottom) S_2 in the north: the effect of throughflow on hysteresis in the system. For a given throughflow value on the x axis, the hysteresis range is shown on the y axis. Upward triangles mark when the system transitions from penetrating to leaping for increasing WBC flow rate. Downward triangles mark when the system transitions from leaping to penetrating for decreasing WBC flow rate. Linear fits and slopes are provided. Error bars represent the flow rate step size.

 $L_{\rm BP}$ are blocked by advection. The breakdown of the branch occurs when the width of the plume becomes comparable with the gap half-width $L_{\rm BP} \approx a$, and thus the asymptotics for this branch are $Q \approx \beta a^3 H_0$ (details provided by Sheremet 2001). Fitting the numerical results showed that the coefficient of proportionality was very close to unity.

When the throughflow is present, we should modify the above balance by adding the mean advection velocity through the gap $[U_{\rm TF}=Q_{\rm TF}/(2aH_0)]$. Therefore, balancing zonal advection with the β effect, the β -plume breakdown condition will be

$$(Q_{\rm DS} - Q_{\rm TF}/2) \approx \beta a^3 H_0, \tag{3}$$

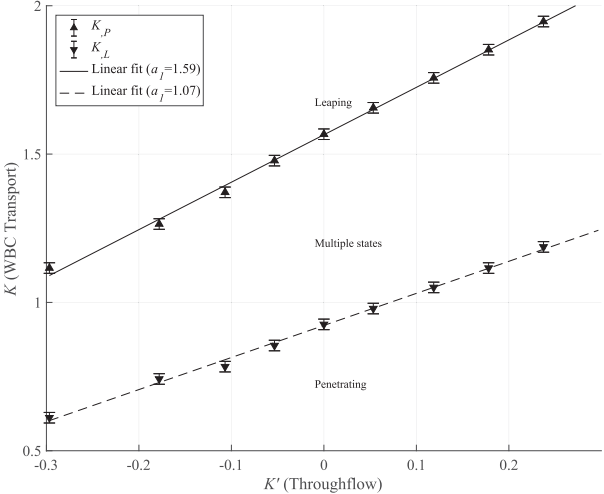


FIG. 7. Numerical model: the effect of throughflow on hysteresis in the system. Results were identical for both source–sink locations S_1 and S_2 .

and it is seen that it is more insightful to consider the dependence on the downstream boundary current transport $Q_{\rm DS} = Q - Q_{\rm TF}$ (Fig. 8). The throughflow, $Q_{\rm TF}$, aids the β effect in promoting the penetration of the flow through the gap. Therefore transport of the boundary current $Q_{\rm DS}$ must be increased in order to switch to a gap leaping state. The actual coefficient of proportionality C between the critical values of the transports $Q_{\rm DS} \approx CQ_{\rm TF}$ may be somewhat different than C=0.5. (or 1.5 for the dependence of Q on $Q_{\rm TF}$). The penetrating branch solution critical $Q_{\rm DS}$ values are shown by upward pointing triangles in Fig. 8. Fitting the data from the laboratory experiment and the numerical solution suggests the range of slope, C, between 0.4 and 0.78 (or between 1.4 and 1.78 for the dependence of Q on $Q_{\rm TF}$).

On the other hand, the breakdown of the flow parallel to the western boundary occurs when the nonlinear terms in the flow traversing the gap become comparable with the β effect, which involves balancing the meridional advection with the β effect. Substituting the scales leads to

$$Q_{DS} \approx \beta L_B^2 a H_0 \tag{4}$$

where L_B is the width of the western boundary current. In Sheremet (2001) it was L_M , the Munk thickness, while in our case L_B is a function of L_M , L_S , and primarily of L_I . Since the throughflow is zonal, we should not expect it to modify the critical condition for the breakdown of the meridional leaping current. The critical $Q_{\rm DS}$ versus $Q_{\rm TF}$ for the breakdown of the gap leaping flow are shown by downward pointing triangles, and indeed do not exhibit much dependence on $Q_{\rm TF}$. The slope of the fitted straight lines is near zero (or 1 for the dependence of Q on $Q_{\rm TF}$).

It is important to note that it is the flow around the downstream tip of the gap that plays a crucial role in the branch breakdowns. It is there that the advection and the beta effect oppose each other, and it is around the downstream tip that the major changes of the flow pattern occur (McMahon et al. 2020, manuscript submitted to *Ocean Modell.*). While the western boundary current transport varies upstream of the gap

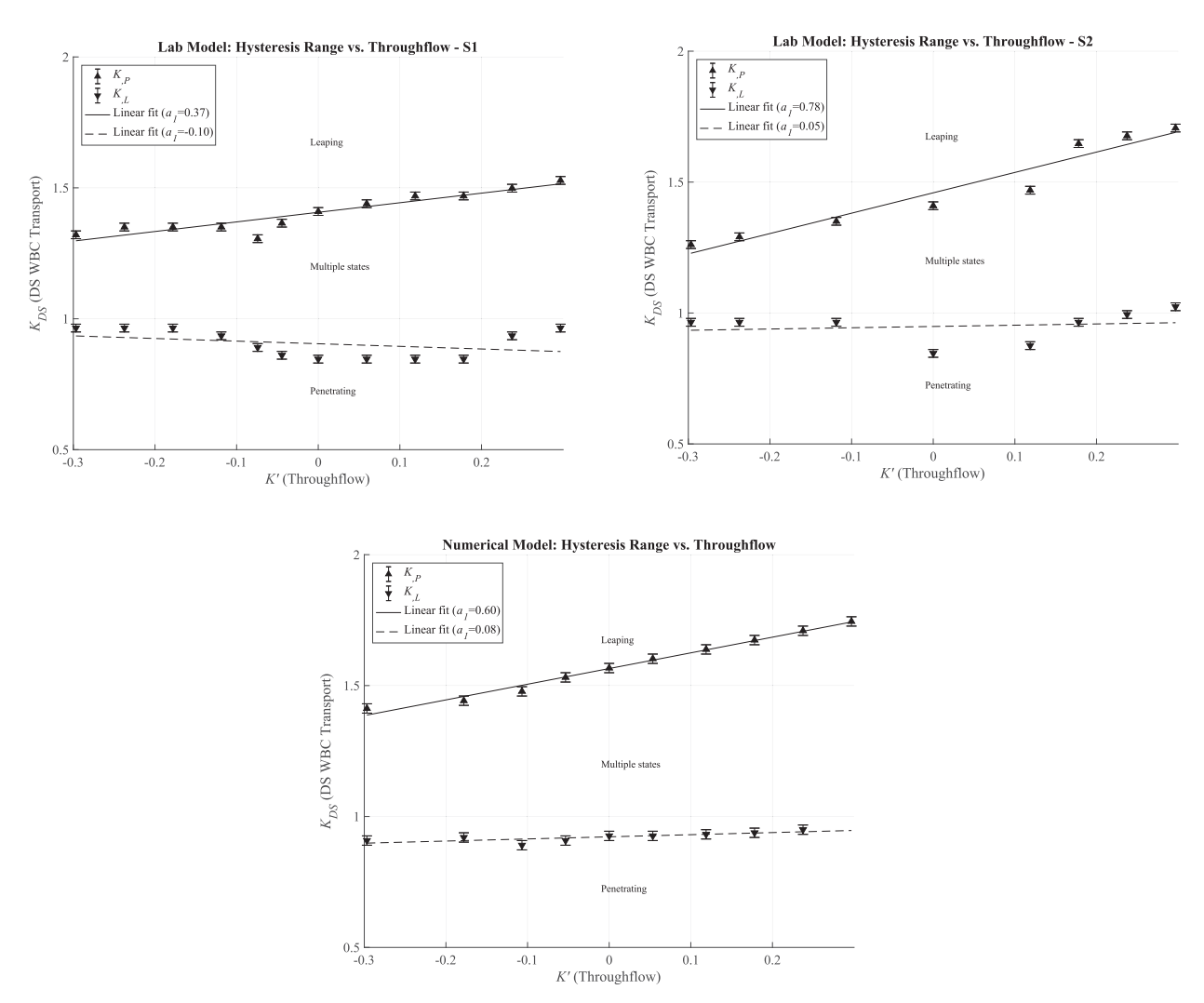


FIG. 8. Laboratory model, source–sink location (top left) S_1 in the south and (top right) S_2 in the north and (bottom) numerical model throughflow results: Q_{DS} against Q_{TF} . Upward triangles mark when the system transitions from penetrating to leaping. Downward triangles mark when the system transitions from leaping to penetrating. Linear fits and slopes are provided. Error bars represent the flow rate step size.

 $Q=Q_{\rm DS}+Q_{\rm TF}$, the excess flows into the western basin, but it is the transport of the boundary current downstream of the gap, $Q_{\rm DS}$, that largely determines the penetrating or leaping state of the system (Fig. 9).

In addition, consider the critical leaping state for zero throughflow. According to Kuehl and Sheremet (2009), transition is expected when the radius of curvature is comparable to the gap half-width, $R_c \approx a$. As the flow decreases, the radius of curvature becomes small enough that the flow wraps around on itself. Figure 10 shows laboratory critical leaping states for the maximum negative and positive throughflow examined, as well as the zero-throughflow case. The negative throughflow permits a larger curvature of the gap-leaping WBC. That is, without this negative throughflow, the current would have wrapped around on itself, forming an eddy which would drift westward and induce transition. Instead, the negative throughflow is effectively preventing eddy formation and drift. The system transitions at a higher flow rate for the positive throughflow case. That is, with

this positive throughflow, it is easier for current to form an eddy which then drifts westward and induces transition. The positive throughflow is effectively enhancing eddy formation and drift. Overall, positive throughflow effectively acts as an increase in the vorticity barrier across the gap, making penetrating states more persistent. Negative throughflow effectively acts as a decrease in the vorticity barrier, making leaping states easier to achieve.

b. Source-sink location

For positive throughflow, weak circulation offshoots from the inflow side of the gap-traversing WBC and broadens toward the western boundary of the basin. For negative throughflow, weak circulation coming from the western boundary converges and connects to the WBC near the outflow side. Comparing the source–sink location for the laboratory model, the linear trends are steeper for S_2 relative to S_1 . This difference is greater for the $K_{,P}$ curve. That is, a throughflow source–sink in the north (S_2) shows an increase effect of throughflow, especially for

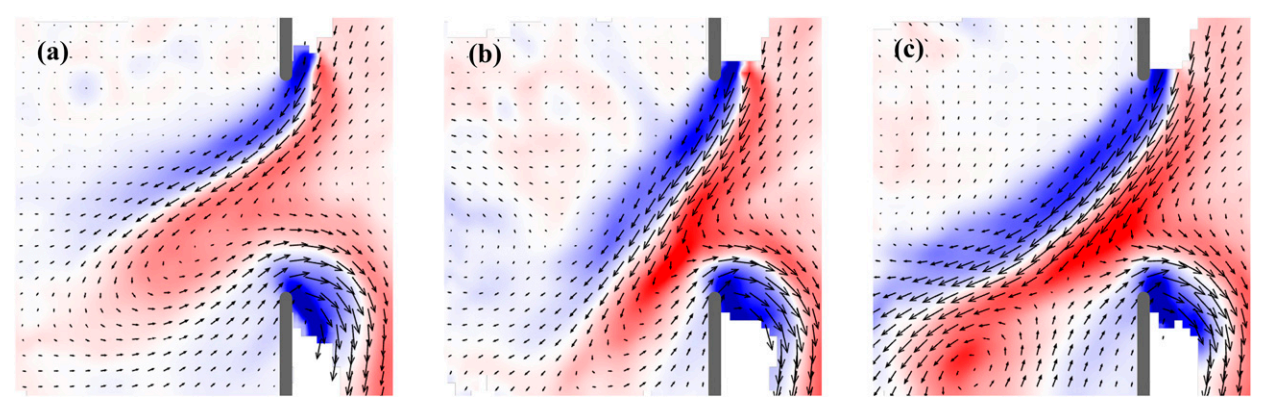


FIG. 9. Critical penetrating states from the laboratory model with source–sink S₂. (a) Negative throughflow ($Q_{TF} = 8 \text{ cm}^3 \text{ s}^{-1}$, $Q = 26 \text{ cm}^3 \text{ s}^{-1}$). (b) Zero throughflow ($Q = 41 \text{ cm}^3 \text{ s}^{-1}$). (c) Positive throughflow ($Q_{TF} = 3.3 \text{ cm}^3 \text{ s}^{-1}$, $Q = 47 \text{ cm}^3 \text{ s}^{-1}$).

penetrating-to-leaping transitions. In the numerical model, however, there is no difference in results for the two sourcesink locations. This is probably due to the steady state nature of the numerical model, via Newton's solution method. Thus, the deviation between numerical and experimental results is likely due to time-dependent eddy shedding processes and possibly to flow instability near the critical transition parameters. Positive throughflow is included in the total inflow WBC and adjusts from the northern portion of the gap before going to the source–sink. The reverse is also true for negative throughflow. That is, the transport lines shooting off of the WBC or gathering toward it are the same, in the numerical model, regardless of if the source–sink is in the north or the south.

c. Model comparisons

The numerical model results were fairly consistent with the laboratory model results. The linear trends in transition WBC flow rates were consistent, as well as their slopes $(K_{,P} \text{ slope} \approx 1 \text{ and } K_{,L} \text{ slope} \approx 1.5$, which is in excellent agreement with the scaling arguments described above). The location of the $K_{,L}$ curve is consistent between models. However, the location of the $K_{,P}$ curve is shifted to higher WBC flow rates for the numerical model compared to the laboratory model. This may be

explained by the difference in nature of the models. The laboratory model is a fully time-dependent model, susceptible to instabilities and periodic eddy shedding. The numerical model uses Newton's method to find a solution, so it is time independent and not affected by flow instabilities that may trigger premature transition. The numerical model is thus able to find solutions to the vorticity-transport function equation that are unstable. The laboratory model is not able to realize unstable solutions, and instability or possibly periodic eddy shedding could trigger transition near critical flow states. As an illustration, Fig. 5 shows a hysteresis trace for the numerical model. As the laboratory model follows the same trace along the penetrating branch, it would transition before reaching the numerical critical state. Flow instabilities may cause the flow state to jump prematurely off the hysteresis fold, despite not reaching the numerical transition flow rate. Instabilities would exacerbate interaction between the opposing jets forming the loop current, especially as the loop becomes smaller nearing critical states. In contrast, the results for $K_{,L}$ are consistent across models, which supports the theory that instabilities do not play a large role in leaping-to-penetrating transitions. Rather, transition is dominated by the competition between inertia and vorticity, and the subsequent curvature formulation of Kuehl and Sheremet (2009).

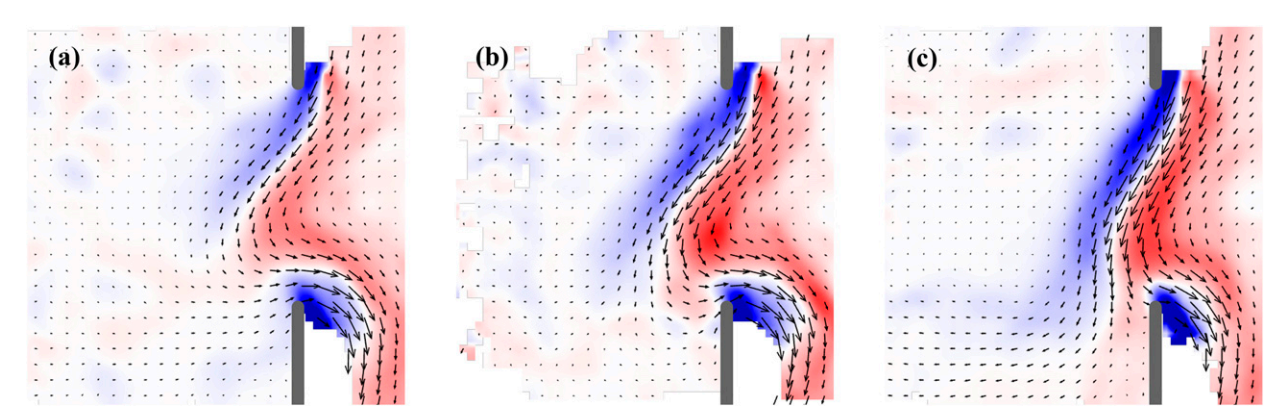


FIG. 10. Critical leaping states from the laboratory model with source-sink S_2 . (a) Negative throughflow ($Q_{TF} = 6.67 \text{ cm}^3 \text{ s}^{-1}$), $Q = 20 \text{ cm}^3 \text{ s}^{-1}$). (b) Zero throughflow ($Q = 26 \text{ cm}^3 \text{ s}^{-1}$). (c) Positive throughflow ($Q_{TF} = 5 \text{ cm}^3 \text{ s}^{-1}$, $Q = 30 \text{ cm}^3 \text{ s}^{-1}$).

5. Summary and conclusions

The goal of this study was to investigate how mean throughflow may affect gap-leaping western boundary currents. Motivated by the Kuroshio intrusion, a simplified laboratory model and an equivalent numerical model were constructed to examine throughflow effects for a single layer system. Simplified gaptraversing WBC models have been studied before and exhibit hysteresis in their flow states (penetrating or leaping) depending on the history of the WBC transport variation.

Both the penetrating-to-leaping (K_{P}) and leaping-topenetrating $(K_{,L})$ transition points of the hysteresis range are significantly affected by throughflow. Positive throughflow shifts the hysteresis range to higher WBC values and widens the hysteresis width. Negative throughflow shifts the hysteresis range to lower WBC values and narrows the hysteresis width. Due to these trends, when the system is near a critical penetrating state, a decrease in throughflow may induce a transition to a leaping state. Additionally, when the system is near a critical leaping state, an increase in throughflow may induce a transition to a penetrating state. These throughflow effects were linear with O(1) proportionality. There was no minimum throughflow magnitude required to have an effect on hysteresis. The results from laboratory model and numerical model were consistent with each other and agree well with an extension of the original scaling analysis of Sheremet (2001). It is important to note that it is the flow around the downstream tip of the gap that plays a crucial role in the branch breakdowns. It is there that advection and the β effect oppose each other, and it is around the downstream tip that the major changes of the flow pattern occur. It is also significant to note the discrepancy between numerical and experimental trends for the penetrating-toleaping transition. This suggests that the specific transition parameters are sensitive to periodic eddy shedding states and/or flow instability. This is in contrast to the leaping-topenetrating transition, suggesting this transition is less sensitive to time dependence and/or flow instability.

Overall, positive throughflow effectively acts as an increase in the vorticity barrier across the gap, making penetrating states more persistent. Negative throughflow effectively acts as a decrease in the vorticity barrier, making leaping states easier to achieve. This result is similar to previous studies, which found that changing select parameters or imposing certain conditions resulted in an upward-shifted hysteresis range as well as an increase in its width: Sheremet (2001) with increasing gap width, Kuehl and Sheremet (2009, 2014) with increasing β effect, Wang et al. (2010) with decreasing meridional wind stress, and Mei et al. (2019) with increasing gap width and/or island width. Additionally, throughflow has been shown here to cause transition when the system is near critical states, much like Yuan and Wang (2011) showed with mesoscale eddy perturbations.

The results of this barotropic study are contrary to the baroclinic work of Song et al. (2019), which found that the mean throughflow must be greater than one-third of the transport of the WBC in order to have an effect. This discrepancy is likely due to difference in system (barotropic versus baroclinic) considered. The linear trends discovered here are valid even for small throughflow deviations from the base zero-throughflow

case; there is no minimum throughflow magnitude required to have an effect on hysteresis. This, combined with the strength of the linear trends, support the need for more consideration of whether the Luzon Strait transport (LST) has a significant effect on the dynamics of the Kuroshio intrusion. The observed South China Sea Branch of the Kuroshio (Caruso et al. 2006) also resembles the positive throughflow leaping case of this study. The LST varies between about 12 Sv westward into the South China Sea and 5 Sv eastward into the Pacific Ocean (Nan et al. 2015). The average LST is between 3 and 6.5 Sv westward. For comparison, the inflow Kuroshio averages a transport of 21 Sv, ranging between about 15 and 25 Sv (Nan et al. 2013). These LST measurements are significant compared to the transport of the Kuroshio, especially given the sensitivity of the simplified models of this study to throughflow. Thus, the climatological shifting of Luzon Strait transport may have a significant impact on the South China Sea circulation.

Acknowledgments. This work was funded by the U.S. National Science Foundation under Award 1823452 and partially by the National Academies of Sciences, Engineering, and Medicine (NASEM) UGOS-1 via Grant 2000009918.

APPENDIX

Traditional Problem Formulation

In the model, various scales exist. The velocity scale is set to the maximum velocity of the WBC measured over all the experimental runs: $U=0.5\,\mathrm{cm\,s^{-1}}$. The defining length scales are the gap width L_g , the gap half-width a, and the western basin width, which is 43.5 cm wide. The depth scale is the layer thickness at the middle of the domain, $H=H_0$, because the fluid is a single layer.

a. Equations of motion

Due to the rapid rotation rate of the experimental tank and the small velocity scale, the Rossby number of the flow will be $R_O = U/2\Omega L \approx 0.032 \ll 1$. Following the standard scaling arguments detailed in Pedlosky (1987), the flow of the single fluid layer will be predominantly two-dimensional and governed by the shallow water equations. The momentum equation is

$$\mathbf{u}_{t} + (f + \omega)\hat{\mathbf{k}} \times \mathbf{u} = -\nabla(p + e) + \nu\nabla^{2}\mathbf{u}, \tag{A1}$$

while the continuity equation is

$$h_{t} + \nabla \cdot (h\mathbf{u}) + \nabla \cdot \mathbf{\Pi}_{F} = 0. \tag{A2}$$

The shallow water equations are valid outside of the viscous layers at the top and bottom of the tank. In Eq. (A1), $\mathbf{u} = u$, v are the depth-independent horizontal velocities in the x and y directions, $f = 2\Omega$ is the Coriolis parameter, $\omega = \nabla \times \mathbf{u}$ is the relative vorticity, p is the pressure anomaly relative to no motion divided by the fluid density (ρ) , $e = \mathbf{u}^2/2$ is kinetic energy per unit mass, and v is the kinematic viscosity. In Eq. (A2), $h(y) = H_0 - 2S_y$ is the fluid layer thickness and Π_E is the Ekman flux. The Ekman flux, defined as $\Pi_E = (1/2)h_E\hat{\mathbf{k}} \times \mathbf{u}$, is a small correction term that accounts for the effect of the

viscous layers of thickness $h_E = \sqrt{2\nu/f} = 0.124$ cm. Its divergence, $\nabla \cdot \Pi_E = -(1/2)h_E\omega$, represents first-order Ekman suction at a solid boundary with Ekman layer depth h_E .

To obtain the general vorticity transport function equation from Eqs. (A1) and (A2), the following steps are applied:

- Define $h\mathbf{u} = \hat{\mathbf{k}} \times \nabla \psi + \nabla \phi$, where ψ and φ are the nondivergent and divergent transport function components, respectively.
- Take the curl of Eq. (A1).
- Substitute the flow divergence $\nabla^2 \phi = -\nabla \cdot \Pi_E = (1/2)h_E \omega$, which is obtained from Eq. (A2) and noting that the fluid layer depth is constant in time.

The general vorticity-transport function equation is then

$$\omega_{t} + J(\psi, q) + \nabla \phi \cdot \nabla q = -q \frac{h_{E}}{2} \omega + \nu \nabla^{2} \omega, \qquad (A3)$$

where $q = (f + \omega)/h$ is the potential vorticity. From Sheremet and Kuehl (2007), $\nabla \phi = (1/2)(h_E/h)\nabla \psi$ can be obtained from combining the definition of the transport function with the Ekman dissipation and expanding in the assumed small term h_E/h . Further steps can be applied to Eq. (A3):

- The Ekman layer vorticity advection is negligible: $\nabla \phi \cdot \nabla q \rightarrow 0$. Physically, this term represents the vorticity advection by the divergent component of the flow field. In the present case, this is the advection of vorticity by the boundary layer which is expected to be small. This can be seen by recalling $\nabla \phi = (1/2)(h_E/h)\nabla \psi$ and noting that the divergent component caused by the Ekman suction is small. For the laboratory case, $\phi/\psi \approx h_E/H = 0.006$ which justifies the approximation.
- Assuming ω ≪ f results in the approximation q ≈ f/h, where q appears explicitly (and not as a derivative).
- The advection term is simplified to be $J(\psi, q) = (1/h)J(\psi, \omega) + \beta(\psi_x/h)$. This results from expanding the Jacobian, applying $\omega \ll f$, and including the topographic β effect $(\beta = 4\Omega S/h \approx 1.3 \text{m}^{-1} \text{s}^{-1})$.

Finally, the vorticity-transport function equation is

$$\omega_t + \frac{1}{h} [J(\psi, \omega) + \beta \psi_x] = -\frac{fh_E}{2h} \omega + \nu \nabla^2 \omega, \qquad (A4)$$

and the relative vorticity in terms of transport function components is a modified Poisson equation,

$$\omega = \nabla \left(\frac{1}{h}\nabla \psi\right) - J\left(\frac{1}{h}, \phi\right). \tag{A5}$$

b. Fundamental balances

Geophysical boundary currents can be characterized by balances between inertia, bottom friction, or lateral friction with β effect. Balancing the advection of relative vorticity with β effect gives the inertial boundary layer thickness

$$L_I = \sqrt{\frac{U_0}{\beta}},\tag{A6}$$

where $U_0 = Q/(H_0L)$ approximates the Sverdrup velocity of the inflow/outflow. Depending on WBC transport, L_I varies

between 1.1 and 2.2 cm over all experiments. Balancing bottom drag with β effect gives the Stommel boundary layer thickness

$$L_{S} = \frac{r}{\beta},\tag{A7}$$

where $r = \Omega h_E/H_0$ is the top and bottom drag. For the experiments, L_S is 0.6 cm. Balancing lateral friction with β effect gives the Munk boundary layer thickness

$$L_M = \left(\frac{\nu}{\beta}\right)^{1/3}.\tag{A8}$$

For the experiments, L_M is 0.9 cm. The model WBC is primarily inertial, especially at medium to high flow rates. From Sheremet (2001), the critical ratio for hysteresis to be present was $a/L_M \ge 4.55$. This is satisfied because the ratio in this experiment was 6.54, so viscous forces are not expected to prevent penetration or hysteresis.

In the present case, the boundary current in the model is traversing a gap. Thus, we are interested in balances that dominate the current between the gap and in the western basin. There are two low inertia balances that describe the penetrating states in which inertia is sufficiently weak, so the boundary current turns into the gap forming primarily zonal flow. The low inertia, steady flow case results in the " β plume" solution (Gill and Smith 1970; Stommel 1982). This solution consists of weak zonal flow in which lateral dispersion balances the β effect. This balance results from Eq. (A4) as

$$\beta \psi_x = -\frac{fh_E}{2h} \psi_{yy} + \nu \psi_{yyyy}. \tag{A9}$$

When Ekman dissipation is dominant over viscosity, the last term in Eq. (A9) can be neglected. The system is then found to admit an analytic similarity solution with error-function structure (details in Kuehl 2014). Extensions of this analytic work to include nonlinearity and stratification can be found in Ibanez et al. (2018) and Kuehl and McMahon (2020), respectively.

The low inertia, unsteady flow case describes the decay of geostrophic flow by Ekman pumping:

$$\omega_t = -\frac{fh_E}{2h}\omega. \tag{A10}$$

This balance leads to the Ekman decay time scale, $T_e = h/\sqrt{\nu\Omega}$. In contrast to the low inertia balances, the high inertia case consists of a gap-leaping configuration where advection balances the β effect:

$$J(\psi,\omega) + \beta\psi_{x} = 0. \tag{A11}$$

This states that potential vorticity is conserved along a streamline. The terms in Eq. (A11) are understood by considering the gap in the ridge as a vorticity barrier that the boundary current must overcome to leap across. If the flow strength is insufficient, the current will turn into the gap forming a penetrating state. The term $J(\psi, \omega)$ is a measure of the inertia working to overcome the vorticity barrier. The term $\beta\psi_x$ can be interpreted as the vorticity barrier. The vorticity barrier must be traversed faster than T_e to justify the neglect of the viscous terms.

REFERENCES

- Caruso, M. J., G. G. Gawarkiewicz, and R. C. Beardsley, 2006: Interannual variability of the Kuroshio intrusion in the South China sea. J. Oceanogr., 62, 559–575, https://doi.org/10.1007/ s10872-006-0076-0.
- Centurioni, L. R., P. P. Niiler, and D. Lee, 2004: Observations of inflow of Philippine Sea surface water into the South China Sea through the Luzon Strait. *J. Phys. Oceanogr.*, **34**, 113–121, https://doi.org/10.1175/1520-0485(2004)034<0113:OOIOPS>2.0.CO;2.
- Farris, A., and M. Wimbush, 1996: Wind-induced Kuroshio intrusion into the South China Sea. J. Oceanogr., 52, 771–784, https://doi.org/10.1007/BF02239465.
- Gill, A. E., and R. K. Smith, 1970: On similarity solutions of the differential equation ψ zzzz + ψ x = 0. *Math. Proc. Cambridge Philos. Soc.*, **67**, 163–171, https://doi.org/10.1017/S0305004100057200.
- Gilmore, R., 1981: *Catastrophe Theory for Scientist and Engineers*. John Wiley and Sons, 696 pp.
- Hsin, Y.-C., C.-R. Wu, and S.-Y. Chao, 2012: An updated examination of the Luzon Strait transport. J. Geophys. Res., 117, C03022, https://doi.org/10.1029/2011JC007714.
- Ibanez, R., J. Kuehl, K. Shrestha, and W. Anderson, 2018: Brief communication: A nonlinear self-similar solution to barotropic flow over varying topography. *Nonlinear Processes Geophys.*, 25, 201–205, https://doi.org/10.5194/npg-25-201-2018.
- Kuehl, J. J., 2014: An analytic solution for barotropic flow along a variable slope topography. *Geophys. Res. Lett.*, 41, 7591–7594, https://doi.org/10.1002/2014GL061188.
- ——, and V. A. Sheremet, 2009: Identification of a cusp catastrophe in a gap-leaping western boundary current. *J. Mar. Res.*, 67, 25–42, https://doi.org/10.1357/002224009788597908.
- —, and —, 2014: Two-layer gap-leaping oceanic boundary currents: Experimental investigation. *J. Fluid Mech.*, **740**, 97– 113, https://doi.org/10.1017/jfm.2013.645.
- ——, and C. McMahon, 2020: An analytic solution for bottom intensified flow along sloping topography. *Eur. J. Mech. B Fluids*, 82, 156–160, https://doi.org/10.1016/j.euromechflu.2020.03.007.
- Lien, R. C., B. Ma, Y. H. Cheng, C. R. Ho, Q. Qiu, C. M. Lee, and M. H. Chang, 2014: Modulation of the Kuroshio transport by mesoscale eddies at the Luzon Strait entrance. *J. Geophys. Res. Oceans*, 119, 2129–2142, https://doi.org/10.1002/2013JC009548.
- Liu, Q., R. Huang, D. Wang, Q. Xie, and Q. Huang, 2006: Interplay between the Indonesian throughflow and the South China Sea throughflow. Chin. Sci. Bull., 51, 50–58, https://doi.org/10.1007/s11434-006-9050-x.
- —, D. Wang, W. Zhou, Q. Xie, and Y. Zhang, 2010: Covariation of the Indonesian throughflow and South China Sea throughflow associated with the 1976/77 regime shift. *Adv. Atmos. Sci.*, 27, 87–94, https://doi.org/10.1007/s00376-009-8061-3.
- McMahon, C. W., J. J. Kuehl, and V. A. Sheremet, 2020: A viscous, two-layer western boundary current structure function. *Fluids*, 5, 63, https://doi.org/10.3390/fluids5020063.
- Mei, H., Y. Qi, B. Qiu X. Cheng, and X. Wu, 2019: Influence of an island on hysteresis of a western boundary current flowing across a gap. J. Phys. Oceanogr., 49, 1353–1366, https://doi.org/ 10.1175/JPO-D-18-0116.1.
- Metzger, E., and H. Hurlburt, 2001: The nondeterministic nature of the Kuroshio penetration and eddy shedding in the South China Sea. *J. Phys. Oceanogr.*, **31**, 1712–1732, https://doi.org/10.1175/1520-0485(2001)031<1712:TNNOKP>2.0.CO;2.
- Nan, F., H. Xue, P. Xiu, F. Chai, M. Shi, and P. Guo, 2011: Oceanic eddy formation and propagation southwest of Taiwan. J. Geophys. Res., 116, C12045, https://doi.org/10.1029/2011JC007386.

- —, —, F. Chai, D. Wang, F. Yu, M. Shi, P. Guo, and P. Xiu, 2013: Weakening of the Kuroshio intrusion into the South China Sea over the past two decades. *J. Climate*, **26**, 8097–8110, https://doi.org/10.1175/JCLI-D-12-00315.1.
- —, and F. Yu, 2015: Kuroshio intrusion into the South China Sea: A review. *Prog. Oceanogr.*, **137**, 314–333, https://doi.org/10.1016/j.pocean.2014.05.012.
- National Academies of Sciences, Engineering, and Medicine, 2018: Understanding and Predicting the Gulf of Mexico Loop Current: Critical Gaps and Recommendations. National Academies Press, 116 pp., https://doi.org/10.17226/24823.
- Nitani, H., 1972: Beginning of the Kuroshio. Kuroshio: Physical Aspects of the Japan Current, H. Stommel and K. Yoshida, Eds., University of Washington Press, 129–163.
- Pedlosky, J., 1987: Geophysical Fluid Dynamics. 2nd ed. Springer, 710 pp.
- Qiu, B., and R. Lukas, 1996: Seasonal and interannual variability of the North Equatorial Current, the Mindanao Current and the Kuroshio along the Pacific western boundary. *J. Geophys. Res.*, **101**, 12 315–12 330, https://doi.org/10.1029/95JC03204.
- Sheremet, V. A., 2001: Hysteresis of a western boundary current leaping across a gap. J. Phys. Oceanogr., 31, 1247–1259, https://doi.org/ 10.1175/1520-0485(2001)031<1247:HOAWBC>2.0.CO;2.
- —, and J. Kuehl, 2007: Gap-leaping western boundary current in a circular tank model. *J. Phys. Oceanogr.*, 37, 1488–1495, https://doi.org/10.1175/JPO3069.1.
- Song, X., D. Yuan, and Z. Wang, 2019: Hysteresis of a periodic or leaking western boundary current flowing by a gap. *Acta Oceanol.* Sin., 38, 90–96, https://doi.org/10.1007/s13131-018-1251-z.
- Stommel, H., 1982: Is the South Pacific helium-3 plume dynamically active? *Earth Planet. Sci. Lett.*, **61**, 63–67, https://doi.org/10.1016/0012-821X(82)90038-3.
- —, and K. Yoshida, 1972: *Kuroshio: Its Physical Aspects*. University of Tokyo Press, 517 pp.
- Wang, Z., D. Yuan, and Y. Hou, 2010: Effect of meridional wind on gap-leaping western boundary current. *Chin. J. Oceanology Limnol.*, 28, 354–358, https://doi.org/10.1007/s00343-010-9281-1.
- Wei, Z., and Coauthors, 2019: An overview of 10-year observation of the South China Sea branch of the Pacific to Indian Ocean throughflow at the Karimata Strait. *Acta Oceanol. Sin.*, **38** (4), 1–11, https://doi.org/10.1007/s13131-019-1410-x.
- Wu, C.-R., and Y.-C. Hsin, 2012: The forcing mechanism leading to the Kuroshio intrusion into the South China Sea. *J. Geophys. Res.*, **117**, C07015, https://doi.org/10.1029/2012JC007968.
- Wyrtki, K., 1961: Physical oceanography of the southeast Asian waters. Scientific Results of Marine Investigations of the South China Sea and the Gulf of Thailand 1959-1961, NAGA Rep., Vol. 2, 195 pp.
- Yaremchuk, M., and T. Qu, 2004: Seasonal variability of the large-scale currents near the coast of the Philippines. J. Phys. Oceanogr., 34, 844–855, https://doi.org/10.1175/ 1520-0485(2004)034<0844:SVOTLC>2.0.CO;2.
- Yuan, D., and Z. Wang, 2011: Hysteresis and dynamics of a western boundary current flowing by a gap forced by impingement of mesoscale eddies. *J. Phys. Oceanogr.*, 41, 878–888, https:// doi.org/10.1175/2010JPO4489.1.
- ——, W. Han, and D. Hu, 2006: Surface Kuroshio path in the Luzon Strait area derived from satellite remote sensing data. J. Geophys. Res., 111, C11007, https://doi.org/10.1029/ 2005JC003412.
- X. Song, Y. Yang, and W. K. Dewar, 2019: Dynamics of mesoscale eddies interacting with a western boundary current flowing by a gap. J. Geophys. Res. Oceans, 4117–4132, https:// doi.org/10.1029/2019JC014949.